Phonon Spectroscopy in Antimony and Tellurium Oxides

Atefeh Jafari,[*,†,‡,¶] Benedikt Klobes,[§] Ilya Sergueev,[‖] Duncan H. Moseley,[⊥] Michael E. Manley,[⊥] Richard Dronskowski,[#,@] Volker L. Deringer,[#,△] Ralf P. Stoffel,[#] Dimitrios Bessas,[‡] Aleksandr I. Chumakov,[‡] Rudolf Rüffer,[‡] Abdelfattah Mahmoud,[†,¶] Craig A. Bridges,[∇] Luke L. Daemen,[††] Yongqiang Cheng,[††] Anibal J. Ramirez-Cuesta,[††] and Raphael P. Hermann[*,⊥,†]

†*Jülich Centre for Neutron Science JCNS and Peter Grünberg Institut PGI, JARA-FIT, Forschungszentrum Jülich GmbH, 52425 Jülich, Germany*

‡*ESRF - The European Synchrotron, 38043 Grenoble Cedex 9, France*

¶*Faculté des Sciences, Université de Liège, B-4000 Liège, Belgium*

§*University of Applied Sciences Bremerhaven, Bremerhaven Institute of Nanotechnology, An der Karlstadt 8, 27568 Bremerhaven, Germany*

‖*Deutsches Elektronen-Synchrotron DESY, D-22607 Hamburg, Germany*

⊥*Materials Science and Technology Division, Oak Ridge National Laboratory, Oak Ridge, TN 37831, USA*

#*Institute of Inorganic Chemistry, RWTH Aachen University, Landoltweg 1, 52056 Aachen, Germany*

@*Hoffmann Institute of Advanced Materials, Shenzhen Polytechnic, 7098 Liuxian Blvd, Nanshan District, Shenzhen, China*

△*Current address: Department of Chemistry, University of Oxford, Oxford OX1 3QR, UK*

∇*Chemical Sciences Division, Oak Ridge National Laboratory, Oak Ridge, TN 37831, USA*

††*Neutron Scattering Division, Oak Ridge National Laboratory, Oak Ridge, TN 37831, USA*

E-mail: atefeh.j87@gmail.com; hermannrp@ornl.gov

Abstract

α-Sb_2O_3 (senarmontite), β-Sb_2O_3 (valentinite), and α-TeO_2 (paratellurite) are compounds with pronounced stereochemically-active Sb and Te lone pairs. The vibrational and lattice properties of each have been previously studied, but often led to incomplete or unreliable results due to modes being inactive in infrared (IR) or Raman spectroscopy. Here, we present a study of the relationship between bonding and lattice dynamics of these compounds. Mössbauer spectroscopy (MS) is used to study the structure of Sb in α-Sb_2O_3 and β-Sb_2O_3, whereas the vibrational modes of Sb and Te for each oxide are investigated using nuclear inelastic scattering (NIS) and further information on O vibrational modes is obtained using inelastic neutron scattering (INS). Additionally, vibrational frequencies obtained by density functional theory (DFT) calculations are compared with experimental results in order to assess the validity of the utilized functional. Good agreement was found between DFT-calculated and experimental density of phonon states with a 7% scaling factor. The Sb-O-Sb wagging mode of α-Sb_2O_3 whose frequency was not clear in most previous studies is experimentally observed for the first time at $\sim$ 340 cm^{-1}. Softer lattice vibrational modes occur in orthorhombic β-Sb_2O_3 compared to cubic α-Sb_2O_3, indicating that the antimony bonds are weakened upon transforming from the molecular α phase to the layer-chained β structure. The resulting vibrational entropy increase of 0.45 ± 0.1 k_B/Sb_2O_3 at 880 K accounts for about half of the α-β transition entropy. The comparison of experimental and theoretical approaches presented here provides a detailed picture of the lattice dynamics in these oxides beyond the zone center and shows that the accuracy of DFT is sufficient for future calculations of similar material structures.

Introduction

Electronic lone pairs can give rise to interesting properties, such as optical activity and nonlinear behavior[1,2], low thermal conductivity[3], and catalytic activity[4]. At the same time, they present interesting challenges for electronic structure calculations. α-Sb_2O_3 (senarmontite), β-Sb_2O_3 (valentinite), and α-TeO_2 (paratellurite) are compounds with pronounced

stereochemically-active Sb and Te lone pairs.[5] In order to understand the structure of these compounds, several experimental and *ab initio* studies have been carried out[6–9] and the role of the lone pair formation in determining the dynamical stability has been assessed[10].

Antimony trioxide (Sb_2O_3) commonly exists in two stable solid forms: cubic senarmontite with space group $Fd\bar{3}m$ and (α-Sb_2O_3), which crystallizes below 570 °C[11], and orthorhombic valentinite with space group $Pccn$ (β-Sb_2O_3), which is predominant above 606 °C up to its melting point at 656 °C[12]. The transition temperature is around 570-606 °C[13]. α-Sb_2O_3 is a cubic molecular crystal (also called island or bridgeless type) composed of Sb_4O_6 cages, space group $P4_12_12$, see the molecular structure shown in Fig. 1a. Each cage is formed of four $E$$SbO_3$ trigonal pyramids, where E represents the non-bonding electron pair of Sb(III) in its $5s^25p^0$ configuration. α-Sb_2O_3 is used for catalysis[14], as fire retardant in many applications such as polymer resins, batteries and textiles[15,16], and in composites with carbon as anode material[17]. The β phase has an orthorhombic unit cell, composed of four connected bent rings of $E$$SbO_3$, but in a layer chained structure instead of a molecular structure[18], see Fig. 1b. β-Sb_2O_3 is an essential component in Sb_2O_3-B_2O_3 glasses that enhances nonlinear optical properties[19–21].

Vibrational properties were mainly investigated by means of Raman and Infrared (IR) spectroscopies. In the early 1970s, a study on α-Sb_2O_3 revealed some bands in a rather poor quality spectrum[22]. In 1993, IR results of gas phase Sb_4O_6 at 1000 K modified some of the former assignments[23]. A further survey using Raman spectroscopy was undertaken to investigate the thermal and vibrational behaviour of antimony trioxides synthesized through thermal treatment[7]. They reported the positions of most of the bands, though without mode assignment. Most band assignments have since been revisited in several other studies[24,25]. In 2004, Gilliam *et al.* claimed that the mode at $\sim$ 87 cm^{-1} was wrongly assigned to the fourth T_2 (F_{2g}) mode[22,24,25] and that based on their calculations this mode is located at $\sim$ 355 cm^{-1}, very close to another mode. Nevertheless, because the mode has been assigned to both translational and T_2 modes[26], its observation and assignment of this mode is debatable.

Despite widespread use of β-Sb_2O_3 in optical glasses due to its non-centrosymmetric structure and high polarizability[19–21], the number of studies on vibrational properties of β-Sb_2O_3 is very limited. A list of Raman and IR active modes has been reported by Cody *et al.*[7], some of which were later assigned by Bahfenne *et al.*[27] The first *ab initio* study of β-Sb_2O_3 was carried out by Gilliam *et al.* using several methods: Hartree-Fock (HF), Møller-Plesset (MP2) and density functional theory (DFT). The best agreement with IR and Raman spectroscopy results were obtained from DFT with a negligible error of 0.8-2.5%[28].

Tellurium dioxide-based glasses exhibit unique features of extraordinary nonlinear optical properties and very large third order optical susceptibility owing to their structure[29–31], similar to β-Sb_2O_3. Paratellurite, or α-TeO_2, is the stable crystalline tetragonal phase of tellurium dioxide in a three dimensional structure[8], as shown in Fig. 1c. The $5s^2$ lone pair of tellurium(IV) leads to a non-centrosymmetric chiral material made of distorted $E$$TeO_4$ trigonal bipyramid units. However, from a crystal-chemistry point of view, α-TeO_2 possesses a form closer to a molecular structure than a framework[8,32,33], where the $E$$TeO_4$ unit consists of a somewhat discrete TeO_2 molecule and two additional binding oxygens that have a larger separation from Te and form bridging bonds[34]. The hyperfine interactions in α-TeO_2 have been investigated by Klobes *et al.*[35] by NFS and yield a quadrupole splitting of 6.68(2) mm/s in good agreement with earlier work by Ullrich *et al.* that reported a quadrupole splitting of 6.77(11) mm/s with a linewidth of 6.42(12) mm/s by employing Mössbauer emission spectroscopy following thermal neutron capture[36]. Raman spectroscopy at room temperature and 85 K reveals most of the vibrational frequencies[6]. Since then, the vibrational properties are well understood and have been exhaustively investigated theoretically and experimentally by conventional spectroscopies[8,32–34,37].

For all three materials, it is interesting to investigate the lattice dynamics related properties from the density of phonon states (DPS) point of view which also yields vibrational modes far from the Brillouin zone center. In order to get a better understanding of the vibrational properties and strength of interatomic bonding in these materials with molecular,

layered, and intermediate structures, we have measured both the partial and total DPS using nuclear inelastic scattering (NIS) and inelastic neutron scattering (INS), respectively. These methods are complementary to the classic Raman or IR spectroscopies because they reveal both Raman and IR active and inactive modes. Acoustic as well as optical phonons, and, more importantly, aspects of lattice thermodynamics can be directly investigated using NIS and INS. In addition, structural information can be obtained by hyperfine spectroscopies. Nuclear resonance scattering techniques have been developed to enable element specific lattice dynamics characterization at ambient and high-pressure and at low temperature[38–40]. Here, we report the vibrational properties and lattice dynamics of α-Sb_2O_3, β-Sb_2O_3, and α-TeO_2 obtained by means of synchrotron radiation-based nuclear resonance scattering and inelastic neutron scattering. The experimental results are compared with DFT calculations and utilized to obtain the contribution of vibrational entropy to the α-Sb_2O_3 to β-Sb_2O_3 phase transition. Additionally, we compare classical energy-domain Mössbauer spectroscopy results with time domain synchrotron-based NFS of α- and β-Sb_2O_3 at low temperature.

Methods

Synthesis

The α-Sb_2O_3 and α-TeO_2 compound powders with high purity are commercially available. β-Sb_2O_3 was synthesized by a previously reported wet chemical method[41]. Sb_2O_5 was synthesized and characterized in Ref.[42] The phase purity of the samples was confirmed by XRD measurement using Cu K_α radiation with a wavelength of 0.154 nm.

For inelastic neutron scattering (INS), larger amounts of samples were needed. For α-Sb_2O_3, we purchased Sb_2O_3 from Sigma-Aldrich (99.99% purity). The x-ray diffraction pattern of the material showed a mixture of the α and β phases. To convert this material to the pure α phase, we loaded 2.5 g of the as-received material in a 23 mL Parr autoclave with a Teflon liner. A solution of NaOH in H_2O (10 mL of a 2.5M solution) was added

and the resulting suspension was stirred briefly. The autoclave was then sealed and kept at 175 °C for 3 days in a convection oven. The material was removed from the autoclave and washed with large amounts of deionized H_2O (Büchner funnel, vacuum filtration) until the filtrate was pH neutral. The recovered Sb_2O_3 material was dried overnight at 40 °C in a vacuum oven. Its diffraction pattern showed pure α-Sb_2O_3. This synthesis was repeated several times to produce enough material for inelastic neutron scattering and to produce β-Sb_2O_3, as described below. For β-Sb_2O_3 we tried two methods. First, a self-propagating metathesis reaction was used to produce β-Sb_2O_3[41]. Briefly, a mixture of $SbCl_3$ and NaOH were ground in an agate mortar for 3 minutes, and the product was washed with water and then ethanol, followed by drying at 60 °C. Several reactions were conducted, and we note that a minor α-Sb_2O_3 impurity was observed as a side product in some reactions. Next, approximately 6 g of α-Sb_2O_3 produced by the method described earlier was placed in a vacuum sealed quartz ampule (10 mm diameter, 60 mm long). The ampule was placed in a stainless steel crucible made with a piece of stainless steel tubing (12 mm diameter, 90 mm long) capped with Swagelok compression tube caps. This assembly was placed in a tube furnace at 625 °C overnight, then quenched in water. The same method was also used by heating commercial Sb_2O_3 directly to 650 °C for several hours, followed by quenching in a bucket of ice water. The recovered material was pure β-Sb_2O_3 for both of the latter routes. A very slight amount of preferred orientation was observed in the x-ray diffraction pattern. We used the water-quenched samples for the INS measurements.

Mössbauer spectroscopy

^{121}Sb Mössbauer spectra were obtained on a constant-acceleration spectrometer using a 300 μCi $Ca^{121m}SnO_3$ source and a Janis SH-850 closed cycle cryostat. The detector was a 2 inch NaI scintillator and the energy discrimination eliminated the Sb-K_α fluorescence, keeping the 37.2 keV line and the iodine escape peak. The velocity calibration was performed with α-Fe at room temperature utilizing a ^{57}Co@Rh source. The Mössbauer spectra discussed

here were obtained using two sets of samples with ∼40 mg/cm^2 and 15 mg/cm^2 of powdered β-Sb_2O_3 and one thin sample, 15 mg/cm^2, of powdered α-Sb_2O_3. The extracted isomer shift is reported with reference to $CaSnO_3$.

Nuclear inelastic scattering and inelastic neutron scattering

The NIS and NFS experiments were performed in 16-bunch mode at the ID18 at the European Synchrotron Radiation Facility (ESRF) in Grenoble, France. α-Sb_2O_3 and α-TeO_2 NIS spectra were obtained using a sapphire backscattering monochromator with energy resolutions of 1.1 and 1.3 meV corresponding to the nuclear transition energies of ^{121}Sb (37.129 keV) and ^{125}Te (35.409 keV), respectively[38]. NIS by β-Sb_2O_3 was measured with an improved resolution of $\sim$ 0.7 meV using the same monochromator. The resolution functions in the NIS spectra were recorded using forward-scattered photons by the NFS detector, which was also used to record the NFS time domain spectrum. The data was collected in about 4.5, 4, and 2 hours for α-Sb_2O_3, β-Sb_2O_3, and α-TeO_2 samples, respectively. The measurements were carried out in a closed cycle cryostat at 30 K estimated through a detailed balance analysis with the Bose-Einstein statistics. That allowed us to compensate for the low Lamb-Mössbauer factor at RT in the NFS measurements and to reduce multiphonon contributions in the NIS measurements. INS data were obtained at 5 K using the inverse time-of-flight spectrometer VISION at the Spallation Neutron Source (SNS) at Oak Ridge National Laboratory (ORNL), USA.

The two synchrotron radiation based nuclear resonance techniques based on the Mössbauer effect that we utilized are NIS and NFS. NIS (also called NRIXS - nuclear resonant inelastic x-ray scattering) is a phonon spectroscopy technique, where an inelastic scattering function is obtained by recording the phonon-assisted nuclear resonance absorption by a Mössbauer active element. NFS is a hyperfine spectroscopy technique (also called Synchrotron Mössbauer Spectroscopy) which provides Mössbauer spectral information in time-domain. Compared to Raman or IR spectroscopy which probe vibrations with symmetry related selection rules and

at the zone center, NIS is an isotope-selective technique and probes vibrations integrated over the Brillouin-zone. The selection rule is that only the vibrational component of the nuclear resonant isotope along the synchrotron beam direction is observed. NFS is very similar to Mössbauer spectroscopy, except that it operates in time- and not energy-domain, does not require a radioactive source -which is replaced by the synchrotron radiation beam-, can take advantage of the focused beam, and does not suffer from parasitic radiation generated in most radioactive sources. However, NFS does not directly yield the isomer shift: only the difference in isomer shift between two species in a sample or between a sample and a reference can be obtained. As example contrasting with the Sb(III) spectra, a spectrum for Sb(V) is shown in Fig. 2. More details and a comparison of NIS, NFS, and Mössbauer spectroscopy are discussed in Ref.[43].

Electronic-structure theory

Density functional theory (DFT) computations were done in the projector augmented-wave (PAW) framework[44] using the Vienna Ab initio Simulation Package (VASP)[45–47]. The convergence criterion was set to $\Delta E < 10^{-8}$ eV·cell^{-1} for electronic cycles and to $\Delta E < 10^{-6}$ eV·cell^{-1} for structural optimizations. The cut-off energy for the plane-wave expansion was 500 eV. Reciprocal space was sampled on dense Monkhorst–Pack grids[48]. The grid sizes were $6 \times 6 \times 6$ for α-Sb_2O_3 and $11 \times 5 \times 9$ for α-Sb_2O_3. The structures of α-Sb_2O_3 and β-Sb_2O_3 were fully optimized with regard to lattice vectors and atomic sites within their given space-group symmetries. The semilocal functional of Perdew, Burke, and Ernzerhof (PBE)[49] was employed together with an a posteriori correction for dispersion interactions[49] as implemented in VASP[50]; the latter corrections have been found necessary for a correct structural and energetic description of van der Waals-type solids[51] such as given by the antimony and tellurium oxides. The phonon computations for α-TeO_2 has been reported by Deringer *et al.*[34], in this work their results are analyzed with more detail using the experimental results. DFT-based simulations of lattice dynamics in the harmonic approximation

were performed using the Parlinski-Li-Kawazoe method[52] as implemented in Phonopy[53]; the interatomic forces were obtained from dispersion-corrected PBE computations with VASP as described above. The present methodological framework has been employed and validated during previous lattice-dynamics studies as reported for crystalline α-TeO_2[34] and GeSe[54], respectively. In fact, in the case of α-TeO_2, the dispersion-corrected PBE method was shown to correctly reproduce the intricate α, β stability ordering, and also yielded thermodynamic quantities in good agreement with experiments[34]. In the present study, the frequencies and symmetry assignments were generated using Phonopy[53]. The densities of phonon states have been calculated on dense meshes of reciprocal space points (α-Sb_2O_3: 16×16×16, β-Sb_2O_3: 29×13×24, α-TeO_2: 26×26×18). The data of the theoretical densities of phonon states have been smoothed by a smearing function, using Phonopy's default sigma value of about 1 meV together with a step size of about 0.5 meV. LO-TO splittings have not been included in the modelling because they mostly affect the phonon branches around the gamma point at the very center of the Brillouin zone. Because NIS and INS data reflects the entire Brillouin zone, this methodology is more straightforward. The assignment of vibrational modes was made by visual inspection using the wxDragon software[55]. Comparison with the experimental density of phonon states indicates that the calculated lattice dynamics is too soft. Consequently, in what follows, we have systematically scaled the energy by 1.07 (i.e. 7% hardening) in a norm-conserving way in order to enable direct comparison with Raman, IR, INS, and NIS frequencies.

Results and discussion

Hyperfine interactions and structure The Mössbauer spectra of α- and β-Sb_2O_3 measured at 90 K and corresponding fits to the data are depicted in Fig. 2a and the derived fitted hyperfine parameters are summarized in Table 1. Spectra obtained at other selected temperatures are in Fig. S1 of the Supplementary Material. The characteristic isomer shifts

indicate that antimony is trivalent Sb(III) in both oxides. The values of -11.6(1) and -11.8(1) mm/s for α- and β-Sb_2O_3, respectively, are in good agreement with litterature, see Table 1 and Ref.[56]. We determined a quadrupole splitting ($\Delta E_Q = eQVzz$) of about 19.0 mm/s for both phases of Sb_2O_3. These values are slightly larger than reported earlier, see Table 1. The stereochemical property of the Sb(III) lone pair in both phases is the origin of the pronounced quadrupole splitting, produced by the large electric field gradient at the nucleus. We estimate an asymmetry parameter, η, of 0.44(3) for β-Sb_2O_3 in agreement with $\eta = 0.36$ measured at 77 K using nuclear quadrupole resonance (NQR) spectroscopy[57,58]. For the α phase, a zero asymmetry parameter is obtained consistent with the three-fold point symmetry of the Sb site and NQR[57] but at variance with another NQR study that reports a tiny $\eta = 0.006$, though without errorbar[58]. NQR also provides values for $\Delta E_Q \sim 18.5$ and 18.1 mm/s for α- and β-Sb_2O_3, respectively[58].

Table 1: Spectral parameters of antimony oxides obtained by Mössbauer spectroscopy and nuclear forward scattering. The isomer shift reference is $CaSnO_3$; thin and thick absorber denoted by ^{t} and ^{T}, respectively

Sample	Method	T(K)	δ(mm/s)	ΔE_Q(mm/s)	η	Γ(mm/s)
α-Sb_2O_3	Mössbauer	90	-11.6(1)	18.8(7)	0	3.1(1)
”	NFS	35	-	17.2(2)	0	-
β-Sb_2O_3	Mössbauer	90^t	-11.8(1)	19.7(4)	0.49(5)	2.9(1)
β-Sb_2O_3	”	90^T	-11.7(1)	19.6(1)	0.34(3)	3.08(3)
”	NFS	35	-	16.9(2)	0.14(3)/0.5(2)	-
α-Sb_2O_3	Mössbauer[59]	77	-11.32(12)	18.3(4)	0	3.14(10)
”	” [60]	77	-11.90(7)	18.2(5)	0	3.07(8)
”	NFS[61]	12	-	17.8(4)	0	-
β-Sb_2O_3	” [62]	20	-11.8(1)	16.9(5)	0	2.8(1)
”	” [59]	77	-11.33(7)	17.0(2)	0	2.89(10)

From several temperature-dependent Mössbauer measurements, one can estimate the temperature dependence of the Lamb-Mössbauer factor (f_{LM}) by modelling the spectral area within the Debye model[63]. This method requires to find the proportionality factor between the area f_{LM}. The temperature dependence of the spectral area for ^{121}Sb-f_{LM} for

α-Sb_2O_3 and β-Sb_2O_3 are shown in Fig. 2b, scaled to either match best Debye behavior in the high-temperature limit (closed points, MS_{hT}) or to match the f_{LM} determined directly from NIS at 35 K (open points, MS_{NIS}). For α-Sb_2O_3 the agreement between models is good and the deviation at the lower temperature can be attributed to saturation effects, as the nuclear thickness strongly increases below 90 K. Comparison between two samples of different thickness for β-Sb_2O_3 shows crude agreement. The thin and thick sample follow the same trend above 150 K, with a Debye temperature of 190 K; below 150 K the thick sample exhibits severe deviations due to saturation whereas in the thin sample saturation appear below 90 K. The high temperature fit yields a Debye temperature of 190(5) K Sb both in α-Sb_2O_3 and β-Sb_2O_3; considering the full temperature range reveals that both materials are not well described by a Debye model. Examining more closely the spectral area evolution for the thin samples further with the extrapolated NIS in the harmonic approximation $f_{LM}(T)$, see Equation 1, reveals a good match for α-Sb_2O_3, but a poor match for β-Sb_2O_3 regardless of the choice of scaling factor. We speculate that anharmonicity is the root cause of this disagreement and warrants deeper investigation beyond the scope of this work. We note that considering only the low temperature behavior or a too thick sample would lead to wrong conclusions.

We also measured the low temperature time-resolved NFS spectra with the ^{121}Sb nuclear transition in α- and β-Sb_2O_3, and for comparison, Sb_2O_5, which features Sb(V) and does not exhibit an electronic lone-pair[42] nor the associated large quadrupole splitting. For the latter, the deviation from a simple exponential decay with the natural lifetime comes from dynamical scattering which is always present in a samples of finite thickness[64]. The spectra and corresponding fits obtained with the CONUSS software[65] are presented in Fig. 2c. The spectra for the trivalent oxides exhibit a quantum-beat pattern associated with the quadrupole hyperfine splitting. In α-Sb_2O_3, the obtained quadrupole splitting of 17.2(2) mm/s is in reasonable agreement with the reported values from Mössbauer spectral measurement, see Table 1. Note that the largest source of error in ΔE_Q values is the still rather poorly defined

ratio of the quadrupole moment of the nuclear ground and excited state for ^{121}Sb which is in the range of 1.31-1.34 and cross-correlation of sample thickness and spectral parameters. For β-Sb_2O_3, a significant thickness distribution prevents us from obtaining a good fit for the entire spectrum (see bottom panel in Fig. 2c). Therefore, we fit the spectrum in two steps: first, a line of best fit for entire time range is shown in black. This fit gives ΔE_Q = 16.9(2) mm/s, a value close to the Mössbauer spectroscopy-based result and the literature[59], and $\eta = 0.14(3)$, which is not in agreement with the Mössbauer result. In the second step, the latter part of the spectrum (15 ns $\leq t \leq$ 35 ns) has been refit, see red line, which is somewhat akin to considering a thinner sample. The derived quadrupole splitting did not change whereas the asymmetry parameter increased to $\sim 0.5(2)$ as compared to the first fit and becomes closer to the Mössbauer spectral fit for the thinner sample. Thickness distribution in the sample is detrimental to obtaining high precision hyperfine parameters for NFS. Generally, a time domain NFS spectrum gives a more accurate quadrupole splitting than classical Mössbauer spectroscopy because the extraction of the quadrupole splitting does not interfere with the large natural line width of ^{121}Sb.

Vibrational properties: Partial Sb and Te DPS The ^{121}Sb and ^{125}Te NIS spectra and their corresponding instrumental functions measured in the respective compounds are shown in Fig. 3. Insets show the same spectra in logarithmic scale. It is worth noting that higher counting statistics were acquired for energies below 60 meV. Due to limited synchrotron measurement time, and the low count rate at high energy, the focus was on data in the low energy region. This is why in insets a and c, the data points higher than 60 meV appear digitized. As the Sb and Te contribution to modes above 60 meV is very small, the relatively poor statistics in this region does not affect the data analysis. The high energy region vibrational modes are better captured by inelastic neutron scattering, see below. The ^{121}Sb-DPS is extracted from NIS spectra by the Fourier-Log decomposition method[66,67], as shown in Fig. 4.

α-Sb_2O_3: The DPS of α-Sb_2O_3 exhibits peaks at 55, 87, 124, 175, 188, 233, 260, 316, 360, 450, 613, and 740 cm^{-1} (for the sake of comparison with the literature, the mode frequencies are given here in wavenumbers instead of the more typical meV). The calculated ^{121}Sb-DPS shows very similar features to the measured DPS in terms of frequency and intensity, as can be seen in Fig. 4. The positions of these bands are summarized and compared to our INS measurements and previous studies in Table 2. The low energy modes appeared as shoulder peaks of the mode 87 cm^{-1} in NIS results. Small differences between the vibrational frequencies from literature and our NIS-based values could be related to the temperature and to the sampling of the full Brillouin-zone rather than the zone center. Small differences with the DFT results that persist after an overall 7% scaling may be due to, for example, more subtle inter-molecular interactions which are not fully accounted for in our calculations.

Most of the modes for α-Sb_2O_3 that we observed were reported in other studies using Raman or IR spectroscopies, but our data reveal important differences and new insights in mode assignment. The bending modes occur at low frequencies up to $\sim$ 200 cm^{-1}, while wagging modes are in the mid-frequency range, 200-400 cm^{-1}, and stretching modes are at higher frequencies starting from $\sim$ 600 cm^{-1}, in agreement with Refs.[18,28]. The first modes up to around 100 cm^{-1} correspond to coherent libration movements of Sb_4O_6 entities. Though often called translational modes in the literature, we use the libration terminology here, as these modes are not to be confused with the translational movement of the whole lattice, which has zero frequency at the zone center. The 87 cm^{-1} band has previously been assigned as a Sb-O-Sb wagging mode in several reports[22,24,25], however our results reveal it as a librational vibration, which agrees with the assignment by Gilliam *et al.*[28]. Instead, this particular Sb-O-Sb wagging mode is found at 316, 340, and 337 cm^{-1} in our NIS-, INS-, and DFT-obtained DPS, respectively. It is located very close to another mode at 360 cm^{-1} as is clearly visible in DFT and INS results, given below. Due to the weak intensity of the former mode and its superposition with the latter, it was not visible or distinguishable in earlier experimental reports using conventional optical spectroscopies[22,24,25,28]. This mode could be

the missing fourth $T_2(F_{2g})$ mode with the expected frequency at 337 cm^{-1} [28].

Our measured DPS also provide the first experimental observation of two additional Raman and IR inactive bands around 175 and 595 cm^{-1}. These modes are predicted to be around at 191 and 590 cm^{-1} based on calculations in Ref. [28]. These peaks appeared with higher intensities in the INS and DFT spectra as compared to NIS one. INS and DFT also reveal a distinct mode around 740 cm^{-1}, which has not been reported earlier in α-Sb_2O_3, however it has been seen in As_4O_6 which has a very similar molecular structure to α-Sb_2O_3 [68,69].

β-Sb_2O_3: The Sb-DPS of β-Sb_2O_3 exhibits peaks at 60, 100, 150, 190, 218, 233, 284, and 446 cm^{-1} (see the middle panel of Fig. 4 and Table 3). According to previous experimental and computational studies [7,24,70], there are additional modes in the $\sim$ 300-650 cm^{-1} range. However, these modes are not visible in our measured Sb-specific DPS due to their low intensity. The modes below 400 cm^{-1} correspond to group modes [7] and the ones above 500 cm^{-1} are related to stretching modes related to SbO_3 units [71]. In the external mode region, the Sb modes in β-Sb_2O_3 shift toward lower energy as compared to α-Sb_2O_3. Considering that group modes (also called lattice or external modes) are vibrations from all atoms in the unit cell and associated with crystal structure and symmetry changes [18,72], this softening can be explained by the modification of the crystal structure from a molecular-type structure in the α phase to a chain structure in the β phase. The larger density of the β phase also rationalizes softening of the external modes. The internal modes correspond to vibrations from the molecules, located in the 400-800 cm^{-1} range and controlled by the Sb-O chains in β-Sb_2O_3 [7]. This seems to indicate that despite the higher density of β-Sb_2O_3, the bonding is weaker in the chain structure as valence electrons are now shared across more atoms, as is also reflected in the force constants, see below. This is reminiscent of the bonding change upon crystallization in $GeSb_2Te_4$ [73], where the amorphous covalent form exhibits harder optical vibrations than the crystalline form with shared valence electrons. These softer than expected vibrational modes are a general feature for shared electrons [74].

α-TeO_2: The analysis of the experimental ^{125}Te-DPS in α-TeO_2 reveals modes at 73, 103, 136, 158, 175, 223, 260, 320, and 406 cm^{-1} with similar frequencies in the DFT-obtained DPS. Table 4 summarizes the position of the modes and their qualitative assignments. The force constant between Te and the axial oxygens in α-TeO_2 is larger than equatorial ones, leading to a shorter axial bond length and the formation of weakly coupled TeO_2 molecules[33]. From our calculations and a study by Rodriguez *et al.*,[37] the vibrations of the Te-$O_{equatorial}$ groups relative to each other show a mixed libration deformation behaviour with frequencies up to $\sim$ 300 cm^{-1}. The librational-deformational bands in 300-400 cm^{-1} range are related to Te-$O_{equatorial}$ and Te-O_{axial}[37].

The librational and deformational (bending) modes are often superimposed, therefore distinguishing single bands in this oxide is rather difficult[6,9,75]. Nonetheless, it is clearly possible to separate the DPS into two regimes: first, a set of librational and/or deformational modes of the TeO_4 unit (up to 400 cm^{-1}) and, second, stretching modes of molecular units (starting at 600 cm^{-1}). The latter modes with weaker intensity are visible in the ^{125}Te-DPS shown in the bottom of Fig. 4, and while the frequencies are consistent with previous studies[6,9,75], the rather weak intensities indicate that these modes do not include strong Te motions.

The partial DPS, $g(E)$, in α-Sb_2O_3, β-Sb_2O_3, and α-TeO_2 reveal the structure-dependent phonon distributions from low to high energies. The NIS data discussed here probes the Sb/Te modes and shows a more molecular nature for α-Sb_2O_3 and α-TeO_2, whereas β-Sb_2O_3 exhibits softening related to the chain-forming structure. The INS discussed below detects all modes with a strong weighting towards O modes.

Vibrational properties: total DPS The calculated total normalized DPS of α-Sb_2O_3, β-Sb_2O_3, and α-TeO_2 are obtained by summing the Sb or Te and O partial DPS, considering the stoichiometric ratio for each oxide, and are compared with the neutron-weighted DPS in Fig. 4. In α-Sb_2O_3, the frequencies obtained by INS and the total DFT

are in general agreement. The total DPS in INS reflects O vibrational modes more than those of Sb or Te. This is expected as the effective weighting is given by σ/M, the ratio of the scattering cross-section to the mass. These values are 0.25, 0.032, and 0.025 barn/amu for O, Sb, and Te, respectively. We note that, strictly speaking, INS data obtained on the VISION spectrometer does not capture the correct density of phonon states, in particular at low energies, because of the limiting sampling in Q-space. In order to obtain the INS pseudo-DOS in Fig. 4 we have applied a procedure described in the Supplementary Material of Ref.[76]. The neutron-weighted DFT DPS that is expected considering the Q-space covering of VISION has been calculated using the OCLIMAX sofware[77] and is shown in comparison with the INS data in Fig. S2 of the Supplementary Material.

The calculated total-DPS for α-TeO_2 is somewhat similar to that of α-Sb_2O_3. As expected, the Te/Sb and O both contribute to the low energy region whereas O vibrations are main contributors to the high energy region. Intense modes emerge in low and high frequency regions whereas the middle frequency region (400-500 cm^{-1}) is mostly gapped. This is a fingerprint of oxides composed of quasi-isolated molecules, e.g. α-Sb_2O_3 and α-TeO_2 or structures with corner-sharing units such as orthosilicate anions in many forms of SiO_2, see e.g. Supplementary Materials in Ref.[78]. In contrast, the middle frequency region of β-Sb_2O_3 is filled with strong bands, mainly due to O vibrations which present both structural and vibrational similarity to other chain structured compounds, e.g. As_2O_3 and Bi_2O_3[79]. Bridging bonds in the TeO_2 structure therefore do not appear to play a prominent role in the vibrational spectrum and indicate that the compound behaves vibrationally more like a a molecular structure.

Lattice thermodynamics Lattice (thermo)dynamic quantities like f_{LM}, the mean force constant F, sound velocity v_s, and atomic displacements $<u^2>$ can be derived directly from the normalized DPS. In Table 5 we present a list of thermodynamic quantities obtained using the NIS element-specific DPS considering the experimental energy ranges which are

Table 2: α-Sb_2O_3 vibrational mode frequencies from the ^{121}Sb-NIS spectrum and DFT-calculated frequencies (with 7% hardening) compared with previous studies. The qualitative assignments of the observed modes are presented. The uncertainty associated with each peak is 3 cm^{-1}.

	Wavenumber (cm^{-1})										
Assignment	NIS	DFT	INS	[7]	[22]	[23]	[24]	[25]	[26]	[28]	
Librational	-	45	40	-	-	-	-	-	-	-	
Librational	55	63	52	-	-	-	-	-	-	-	
Librational	87	86	95	84	87	87	82	87	85	-	
Sb-O-Sb bend	124	125	124	124	121	121	118	120	120	121	
Sb-O-Sb wag	175	175	176	-	-	-	-	-	-		
Sb-O-Sb bend	188	195	188	197	193	176	189	192	191	190	
Sb-O-Sb wag	233	228	238	-	-	-	-	-	-	-	
Sb-O-Sb wag	260	262	256	261	259	256	254	256	255	253	
Sb-O-Sb wag	316	337	340	-	-	-	-	-	-	-	
Sb-O-Sb wag	360	367	360	364	359	359	355	375	358	355	
Sb-O-Sb wag	-	385	383	381	376	-	373	375	374	373	
Sb-O-Sb stretch	450	450	455	458	452	482	450	453	452	451	
Sb-O-Sb stretch	-	595	597	-	-	-	-	-	-	-	
Sb-O-Sb stretch	613	628	620	675	-	-	-	-	-	-	-
Sb-O-Sb stretch	740	730	728	740	717	785	712	715	715	709	
Sb-O-Sb stretch	-	790	785	-	-	-	-	-	-	-	

compared with calculated values extracted from the full range of DPS. The calculated v_s, and C_V are determined from the DFT-computed DPS while f_{LM} and $<u^2>$ are derived from phonon calculations with phonon statistics applied for a temperature corresponding to the respective experimental value. The F quantities are also derived from phonon atomic displacement calculations, as described elsewhere[80].

The speed of sound, v_s, corresponds to the average group velocity for acoustic phonons obtained from Debye levels (the limit of $g(E)/E^2$ for $E \to 0$), extrapolating from the low-energy region in the partial DPS[81]. The corresponding Debye levels of DFT and INS spectra are shown in the insets to Fig. 4. The speed of sound obtained from the element-specific DPS are v_s of 1.90(5), 1.95(5), and 2.20(10) km·s^{-1} for α-Sb_2O_3, β-Sb_2O_3, and α-TeO_2, respectively. These results are close to the DFT-derived quantities of 1.96, 1.70, and 2.22 km·s^{-1}, respectively. In the case of α-TeO_2, our result is substantially larger than 1.90 km·s^{-1} at 30 °C for α-TeO_2 reported in Ref.[82], possibly because obtaining the average speed

of sound from single crystal data is complex, in particular for a highly anisotropic material.

Further, we estimated the area of the acoustic energy cut-off (E_A) for the molecular structural compound, α-Sb_2O_3, according to,[81] $M_R/M_{Total} = \int_0^{E_A} g(E)dE$, where M_R and M_{Total} are the mass of the resonant atom and the total mass of the molecule, respectively. By assuming the total mass of sixteen formula units of Sb_2O_3 for α-Sb_2O_3, we obtained an E_A of $\sim$ 3-4 meV for α-Sb_2O_3. The approximate values are due to the very complex phonon band structure in such molecular structure materials. As seen in the calculated phonon dispersion of α-Sb_2O_3,[10] the acoustic and optical modes coexist at $E < 10$ meV.

Table 3: β-Sb_2O_3 vibrational mode frequencies (ν) from the ^{121}Sb-NIS spectrum and calculated frequencies (with 7% hardening) compared with previous studies. The modes below 400 cm^{-1}, i.e. Group† modes, are controlled by the unit cell and crystal space group of the structure, and modes above 400 cm^{-1} are Sb-O chain stretching modes from the SbO_3 units.[18,83] The uncertainty associated with each peak is 3 cm^{-1}.

	Wavenumber (cm^{-1})						
Assignment[18,83]	NIS	DFT	INS	[7]	[13]	[24]	[71]
Group†	-	38	34	-	-	-	-
	-	57	52	-	-	-	-
	60	70	60	71	-	-	-
	100	102	100	103	-	-	109
	-	123	119	-	139	-	-
	150	148	151	140	-	141	149
	190	191	181	194	186	189	193
	218	220	218	223	213	219	225
	233	233	227	-	223	-	-
	-	255	250	269	254	-	-
	-	273	270	-	-	-	-
	284	288	285	294	291	295	-
	-	330	328	-	-	-	301
Bending	-	415	418	-	-	-	449
	446	460	470	449	440	-	473
	-	514	520	502	496	500	505
Stretching	-	577	581	585	-	-	-
	-	615	625	602	594	596	591
	-	680	690	690	681	-	692

The probability of the recoilless absorption, the Lamb-Mössbauer factor, f_{LM}, obtained from the DPS[66], are summarized in Table 5. We note some disagreement between DFT and

NIS only for β-Sb_2O_3, which we also ascribe to anharmonicity. The DPS were also utilized to calculate f_{LM} as function of temperature in the harmonic approximation,[84] obtained by calculating

$$f_{LM}(T) = \exp\left(-E_R \int_0^\infty \frac{g(E)}{E} \cdot \frac{1+\exp(-E/\mathrm{k_B}T)}{1-\exp(-E/\mathrm{k_B}T)} dE\right), \quad (1)$$

where E_R is the recoil energy, for comparison with the Mössbauer spectral area information for the antimony oxides, as shown in Fig. 2(c). The mean atomic displacement parameter is directly related to f_{LM} with $<u^2> = -\frac{ln f_{LM}}{k^2}$,[84] where k is the photon wave vector of an incident x-ray beam and is a function of energy.

An important lattice related property, the mean force constant, F, which quantifies the average curvature of the potential in which an atom vibrates and thus also the bond strength, can be extracted from $g(E)$ from the following equation:

$$< F >= \frac{M_R}{\hbar^2} \int_0^\infty g(E) E^2 dE. \quad (2)$$

As F is obtained from the second moment of the DPS, it is dominated by optical phonons[73]. Considering the experimental energy ranges for each oxide in the measured DPS, Eq. 2 yields $F_{Sb/Te}$ (α-Sb_2O_3) = 230(15) N/m, F(β-Sb_2O_3) = 168(20) N/m, and F(α-TeO_2) = 225(30) N/m. These values are larger than the DFT values when considering the same energy ranges (see Table 5) but close when consider the scaling factor of 1.07. The impact of high-energy modes can not be neglected, therefore we also calculated the mean force constant by considering the full energy range given by DFT, results which are given as $F[0-Et]$ in the same table. As expected, higher F are achieved for all the oxides as compared to the limited energy range. The force constants reflect that the Sb-O bonding in α-Sb_2O_3 is stronger than in β-Sb_2O_3.

Another derived thermodynamic parameter is the Debye temperature, θ_D. It represents the temperature at which all vibrational modes in a solid are excited and can be derived

Table 4: α-TeO_2 vibrational mode frequencies from the ^{125}Te-NIS spectrum and calculated (with 7% hardening) of ^{125}Te-DPS compared with previous studies. The mode type assignment the observed modes is presented. L. and D. are abbreviation for librational and deformational modes, respectively. The uncertainty associated with each peak position is 3 cm^{-1}.

	Wavenumber (cm^{-1})				
Assignment	NIS	DFT	INS	[6]	[75]
	-	70	70	62	-
	73	81	85	-	76
L.	103	109	106	-	124
	136	141	136	-	-
	158	161	156	157	-
	175	184	178	179	-
	223	232	235	235	-
	260	285	288	281	-
L. D.	320	323	320	-	325
	-	340	340	-	336
	-	362	367	-	379
	-	390	390	391	-
	406	415	415	415	-
	-	604	-	-	644
	-	624	630	649	-
Stretch	-	715	727	-	-
	-	770	-	774	-
	-	794	802	786	-

from the density of phonon states[85]. Here we use the Debye temperature value obtained from the (-2)-moment of the DPS, as defined in Ref.[86,87] which is weighted as the atomic displacement parameters and Lamb-Mössbauer factor. The NIS-extracted value for α-Sb_2O_3 is 208(10) K in fair agreement with 192 K from DFT, respectively. It is close to the earlier reported 198 K for Sb_2O_3-Na_2O-ZnO glass composed of 90% β-Sb_2O_3[88]. The Sb-specific θ_D of 170(10) K and 185 K are determined for β-Sb_2O_3 from NIS and DFT, respectively. In case of α-TeO_2, the Te-specific θ_D of 235(20) K is comparable with the reported values of 249 K[89], 232(7) K[70], and 232 K[82].

Furthermore, from the NIS-measured phonon density of states, we obtained the specific heat capacity, C_V, as it has been described in Ref.[84], and compared them with calculated values by considering the same energy range as the NIS result. The element-specific $C_V(T)$

Table 5: List of the parameters including: sound velocity v_s, Lamb-Mössbauer factor f_{LM}, mean square atomic displacement parameters $<u^2>$, mean force constant F, and heat capacity C_V. The values are derived from NIS and DFT. The F and C_V values are obtained considering experimental energy range (Ec) and entire energy range from DFT (Et). The experimental energy range is $\sim$ 50, 40 and 50 meV for α-Sb_2O_3, β-Sb_2O_3 and α-TeO_2, respectively. The rest of parameters are valid for both ranges. The scaling by 1.07 for DFT was not applied in this table.

Material		T (K)	v_s (km/s)	f_{LM}	$<u^2>$ (10^{-3}Å^2)	F_{Ec} (N/m)	F_{Et}	$C_{V(Ec)}$ ($\mathrm{Jmol^{-1}K^{-1}}$)	$C_{V(Et)}$
α-Sb_2O_3	NIS	35	1.90(5)	0.52(3)	1.8(2)	230(15)	-	6.3(2)	-
	DFT		1.96	0.53	1.8	214	297	6.4	6.3
β-Sb_2O_3	NIS	35	1.95(5)	0.50(5)	1.9(3)	168(20)	-	5.5(5)	-
	DFT		1.70	0.34	2.5	145	266	6.9	6.5
α-TeO_2	NIS	30	2.20(10)	0.65(1)	1.1(3)	225(30)	-	4.0(5)	-
	DFT		2.22	0.63	1.3	205	354	4.3	4.1

of 6.3(2), 5.5(5), and 4.0(5) $\mathrm{J{\cdot}mol^{-1}K^{-1}}$ are obtained for α-Sb_2O_3, β-Sb_2O_3, and α-TeO_2, respectively. Results are in fair agreement with DFT. We also applied the full energy ranges from DFT for evaluation of C_V in the same manner as explained for F. The values did not change significantly as compared to the C_V using the experimental range (see Table 5). We know from the Debye approximation that the specific heat is inversely proportional to the Debye temperature, $C_V \sim (\frac{T}{\theta_D})^3$,[90] so the maximum θ_D yields the minimum C_V for α-TeO_2.

Finally, we use the changes in the DPS between α-Sb_2O_3 and β-Sb_2O_3 to estimate the vibrational entropy contribution to the transition entropy at 880 K (phase stability limit). The vibrational entropy difference per atom from the DPS normalized to unity is given by

$$S^{\beta}_{vib} - S^{\alpha}_{vib} = 3k_B \int_0^{E_{max}} [(n+1)ln(n+1) - nln(n)](g^{\beta}(E) - g^{\alpha}(E))dE, \quad (3)$$

where $n(E,T)$ is the Bose-Einstein occupation factor. Using the total DPS determined from the experimentally validated DFT calculation (Fig. 4) we obtain a vibrational entropy change of 0.45 ± 0.1 k_B per Sb_2O_3 formula unit, evaluated at 880 K. This accounts for about half of the reported total transition entropy of 0.83 k_B per Sb_2O_3 formula unit[91]. Most of this vibrational entropy is derived from the shifts in the oxygen mode DPS above 40 meV,

as seen in Fig. 4.

Conclusion

We have investigated the vibrational properties and lattice dynamics of phase-pure α-Sb_2O_3, β-Sb_2O_3, and α-TeO_2 containing Sb(III) and Te(IV) lone pair elements. The results provide detailed insights into the finite-temperature behavior of these technologically relevant materials and are important for benchmarking DFT lattice dynamics calculations in these systems that feature lone pair electrons. The measured partial DPS obtained from NIS are in excellent agreement with the DFT-calculated once a uniform 7% scaling factor is applied. This indicates that except for a general scaling factor, the internal and external vibrational modes are properly captured by our computational approach. For each oxide the band frequencies obtained from NIS and INS were in good agreement with the earlier studies, but also reveal Raman and IR inactive modes. Additionally, the high resolution NIS results have produced a series of thermodynamic parameters and detect the debated Sb-O-Sb wagging band in α-Sb_2O_3 around 340 cm^{-1} that confirms the signal at 87 cm^{-1} is attributed to librational vibrations, where some earlier reports provided incorrect assignments due to experimental limitations and selection rules. Mössbauer data of α-Sb_2O_3 and β-Sb_2O_3 agree well with previously-reported values but also indicate that for β-Sb_2O_3 a future detailed investigation of anharmonicity is warranted. NFS spectra of the antimony oxides enable greater confidence in the quadrupole splitting values, as they have higher resolution than Mössbauer spectra. Finally, we have derived from our data and calculations that lattice vibrations -in particular oxygen modes- play an important role in the thermodynamics of the phase transition between α-Sb_2O_3 and β-Sb_2O_3, as they contribute half of the reported total transition entropy.

Supporting information

The Supporting Information is available free of charge at https://pubs.acs.org/address here.

Mössbauer spectra of the thin (15 mg/cm^2) and thick (40 mg/cm^2) antimony oxide samples at selected temperatures (Figure S1). The experimental and calculated *neutron weighted* density of phonon states for α-Sb_2O_3, β-Sb_2O_3, and α-TeO_2 (Figure S2).

Acknowledgement

We thank Dres. Lucas Lindsay, Valentino Cooper, and Thomas Watkins for reviewing the manuscript, Dr. Elizabeth Sobalvarro Converso and Prof. Peter Khalifah for provision of Sb_2O_5 powder, and Dr. Ronnie Simon with help for valentinite synthesis.

Material synthesis work by CAB and inelastic neutron scattering work by RPH, MEM, and DHM, and Mössbauer spectral work by RPH was supported by the US Department of Energy, Office of Science, Office of Basic Energy Sciences, Materials Sciences and Engineering Division. Work by LLD (INS and synthesis), YC and AJRC (INS) was supported by was supported by the United States Department of Energy, Office of Science, Office of Basic Energy Sciences, Scientific User Facilities Division, both under Contract Number DE-AC05-00OR22725. We are grateful to the Helmholtz Association of German Research Centres and the Russian Academy of Sciences for supporting the projects HRJRG-402 "Sapphire ultra-optics for synchrotron radiation" and DFG SFB-917 "Nanoswitches".

We thank Mr. Jean-Philippe Celse for technical assistance during data acquisition at ID18. We acknowledge the ESRF for the provision of synchrotron radiation beamtime at ID18 and DESY for provision of synchrotron beamtime at P01. A portion of this research (inelastic neutron scattering at VISION) used resources at the Spallation Neutron Source, a DOE Office of Science User Facility operated by Oak Ridge National Laboratory.

References

(1) Kim, S.-H.; Yoko, T.; Sakka, S. Linear and Nonlinear Optical Properties of TeO_2 Glass. *J. Am. Ceram. Soc.* **1993**, *76*, 2486–2490.

(2) Berkaïne, N.; Orhan, E.; Masson, O.; Thomas, P.; Junquera, J. Nonlinear optical properties of TeO_2 crystalline phases from first principles. *Phys. Rev. B* **2011**, *83*, 245205.

(3) Nielsen, M. D.; Ozolins, V.; Heremans, J. P. Lone pair electrons minimize lattice thermal conductivity. *Energy Environ. Sci.* **2013**, *6*, 570–578.

(4) Walsh, A.; Payne, D. J.; Egdell, R. G.; Watson, G. W. Stereochemistry of post-transition metal oxides: revision of the classical lone pair model. *Chem. Soc. Rev.* **2011**, *40*, 4455–4463.

(5) Atanasov, M.; Reinen, D. Predictive Concept for Lone-Pair Distortions - DFT and Vibronic Model Studies of $AX_n^{-(n-3)}$ Molecules and Complexes (A = N^{III} to Bi^{III}; X = F^{-I} to I^{-I}; n = 3-6). *J. Am. Chem. Soc.* **2002**, *124*, 6693–6705.

(6) Pine, A. S.; Dresselhaus, G. Raman Scattering in Paratellurite, TeO_2. *Phys. Rev. B* **1972**, *5*, 4087–4093.

(7) Cody, C. A.; DiCarlo, L.; Darlington, R. K. Vibrational and thermal study of antimony oxides. *Inorg. Chem.* **1979**, *18*, 1572–1576.

(8) Ceriotti, M.; Pietrucci, F.; Bernasconi, M. *Ab initio* study of the vibrational properties of crystalline TeO_2: The α, β, and γ phases. *Phys. Rev. B* **2006**, *73*, 104304.

(9) Cornette, J.; Merle-Méjean, T.; Mirgorodsky, A.; Colas, M.; Smirnov, M.; Masson, O.; Thomas, P. Vibrational spectra of rhombohedral TeO_3 compared to those of ReO_3-like proto-phase and α-TeO_2 (paratellurite): lattice dynamic and crystal chemistry aspects. *J. Raman Spectrosc.* **2011**, *42*, 758–764.

(10) Matsumoto, A.; Koyama, Y.; Togo, A.; Choi, M.; Tanaka, I. Electronic structures of dynamically stable As_2O_3, Sb_2O_3, and Bi_2O_3 crystal polymorphs. *Phys. Rev. B* **2011**, *83*, 214110.

(11) Bozorth, R. M. The crystal structures of the cubic forms of arsenious and antimonous oxides. *J. Am. Chem. Soc.* **1923**, *45*, 1621–1627.

(12) Buerger, M.; Hendricks, S. The Crystal Structure of Valentinite (Orthorhombic Sb_2O_3). *Z. Kristallogr. Cryst. Mater.* **1938**, *98*, 1–6.

(13) Orman, R. G. Phase Transitions in Antimony Oxides and Related Glasses. Ph.D. thesis, University of Warwick, Coventry, England, 2005.

(14) Kokkalas, D. E.; Bikiaris, D. N.; Karayannidis, G. P. Effect of the Sb_2O_3 catalyst on the solid-state postpolycondensation of poly(ethylene terephthalate). *J. Appl. Polym.* **1995**, *55*, 787–791.

(15) Naidu, B.; Pandey, M.; Sudarsan, V.; Vatsa, R.; Tewari, R. Photoluminescence and Raman spectroscopic investigations of morphology assisted effects in Sb_2O_3. *Chem. Phys. Lett.* **2009**, *474*, 180–184.

(16) Liu, Y.; Wang, H.; Yang, K.; Yang, Y.; Ma, J.; Pan, K.; Wang, G.; Ren, F.; Pang, H. Enhanced Electrochemical Performance of Sb_2O_3 as an Anode for Lithium-Ion Batteries by a Stable Cross-Linked Binder. *Applied Sciences* **2019**, *9*, 2677.

(17) Palanisamy, M.; Pol, V.; F. Evansn, S.; Jackson, K.; Jafta, C. J.; Bridges, C. A.; Dai, S.; Levine, A. M.; Lee, R. J.; Paranthaman, M. P. Encapsulated Sb and Sb_2O_3 Particles in Waste-Tire Derived Carbon as Stable Composite Anodes for Sodium-Ion Batteries. *Sustain. Energy Fuels* **2020**, *4*, 3613–3622.

(18) Nalin, M.; Messaddeq, Y.; Ribeiro, S. J. L.; Poulain, M.; Briois, V.; Brunklaus, G.;

Rosenhahn, C.; Mosel, B. D.; Eckert, H. Structural organization and thermal properties of the Sb_2O_3-$SbPO_4$ glass system. *J. Mater. Chem.* **2004**, *14*, 3398–3405.

(19) Hall, D. W.; Newhouse, M. A.; Borrelli, N. F.; Dumbaugh, W. H.; Weidman, D. L. Nonlinear optical susceptibilities of high-index glasses. *Appl. Phys. Lett.* **1989**, *54*, 1293–1295.

(20) Chagraoui, A.; Yakine, I.; Tairi, A.; Moussaoui, A.; Talbi, M.; Naji, M. Glasses formation, characterization, and crystal-structure determination in the Bi_2O_3-Sb_2O_3-TeO_2 system prepared in an air. *J. Mater. Sci.* **2011**, *46*, 5439–5446.

(21) Petkova, P.; Soltani, M. T.; Petkov, S.; Tacheva, J.; Nedkov, V. Visible and far-infrared spectroscopic studies of Co-doped (80–x)Sb_2O_3–20Na_2O–$x$$WO_3$ glasses. *Phys. Scr.* **2012**, *2012*, 014057.

(22) Beattie, I. R.; Livingston, K. M. S.; Ozin, G. A.; Reynolds, D. J. Single-crystal Raman spectra of arsenolite (As_4O_6) and senarmonite (Sb_4O_6). The gas-phase Raman spectra of P_4O_6, P_4O_{10}, and As_4O_6. *J. Chem. Soc. A* **1970**, 449–451.

(23) Konings, R.; Booij, A.; Cordfunke, E. The infrared spectrum of gaseous Sb_4O_6. *Chem. Phys. Lett.* **1993**, *210*, 380–383.

(24) Mestl, G.; Ruiz, P.; Delmon, B.; Knozinger, H. Sb_2O_3/Sb_2O_4 in reducing/oxidizing environments: an in situ Raman spectroscopy study. *J. Phys. Chem.* **1994**, *98*, 11276–11282.

(25) Degen, I.; Newman, G. Raman spectra of inorganic ions. *Spectrochim. Acta A* **1993**, *49*, 859–887, Applications of fourier transform Raman spectroscopy 3-III.

(26) Pereira, A. L. J.; Gracia, L.; Santamaría-Pérez, D.; Vilaplana, R.; Manjón, F. J.; Errandonea, D.; Nalin, M.; Beltrán, A. Structural and vibrational study of cubic Sb_2O_3 under high pressure. *Phys. Rev. B* **2012**, *85*, 174108.

(27) Bahfenne, S.; Frost, R. L. Vibrational Spectroscopic Study of the Antimonate Mineral Stibiconite. *Spectrosc. Lett.* **2010**, *43*, 486–490.

(28) Gilliam, S. J.; Jensen, J. O.; Banerjee, A.; Zeroka, D.; Kirkby, S. J.; Merrow, C. N. A theoretical and experimental study of Sb_4O_6: vibrational analysis, infrared, and Raman spectra. *Spectrochim. Acta A* **2004**, *60*, 425–434.

(29) Blanchandin, S.; Marchet, P.; Thomas, P.; Champarnaud-Mesjard, J. C.; Frit, B.; Chagraoui, A. New investigations within the TeO_2-WO_3 system: phase equilibrium diagram and glass crystallization. *J. Mater. Sci.* **1999**, *34*, 4285–4292.

(30) Berkaïne, N.; Orhan, E.; Masson, O.; Thomas, P.; Junquera, J. Nonlinear optical properties of TeO_2 crystalline phases from first principles. *Phys. Rev. B* **2011**, *83*, 245205.

(31) El-Mallawany, R. *Tellurite Glasses Handbook: Physical Properties and Data, Second Edition*; CRC Press, 2016.

(32) Thomas, P. A. The crystal structure and absolute optical chirality of paratellurite, α-TeO_2. *J. Phys. C* **1988**, *21*, 4611.

(33) Mirgorodsky, A.; Merle-Méjean, T.; Champarnaud, J.-C.; Thomas, P.; Frit, B. Dynamics and structure of TeO_2 polymorphs: model treatment of paratellurite and tellurite; Raman scattering evidence for new γ- and δ-phases. *J. Phys. Chem. Solids* **2000**, *61*, 501–509.

(34) Deringer, V. L.; Stoffel, R. P.; Dronskowski, R. Thermochemical Ranking and Dynamic Stability of TeO_2 Polymorphs from Ab Initio Theory. *Cryst. Growth Des.* **2014**, *14*, 871–878.

(35) Klobes, B.; Barrier, N.; Vertruyen, B.; Martin, C.; Hermann, R. P. Quadrupole splitting and isomer shifts in Te oxides investigated using nuclear forward scattering. *Hyperfine Interact.* **2014**, *226*, 713–719.

(36) Ullrich, J.; Vincent, D. Te^{125} Mössbauer effect study of neutron capture effects in PbTe, Te and TeO_2. *Journal of Physics and Chemistry of Solids* **1969**, *30*, 1189 – 1195.

(37) Rodriguez, V.; Couzi, M.; Adamietz, F.; Dussauze, M.; Guery, G.; Cardinal, T.; Veber, P.; Richardson, K.; Thomas, P. Hyper-Raman and Raman scattering in paratellurite TeO_2. *J. Raman Spectrosc.* **2013**, *44*, 739–745.

(38) Sergueev, I.; Wille, H.-C.; Hermann, R. P.; Bessas, D.; Shvyd'ko, Y. V.; Zajac, M.; Rüffer, R. Milli-electronvolt monochromatization of hard X-rays with a sapphire backscattering monochromator. *J. Synchrotron Radiat.* **2011**, *18*, 802–810.

(39) Jafari, A.; Sergueev, I.; Bessas, D.; Klobes, B.; Roschin, B. S.; Asadchikov, V. E.; Alexeev, P.; Härtwig, J.; Chumakov, A. I.; Wille, H.-C.; et al., Rocking curve imaging of high quality sapphire crystals in backscattering geometry. *J. Appl. Phys.* **2017**, *121*, 044901.

(40) Sergueev, I.; Glazyrin, K.; Herrmann, M. G.; Alexeev, P.; Wille, H.-C.; Leupold, O.; May, A. F.; Pandey, T.; Lindsay, L. R.; Friese, K.; et al., High-pressure nuclear inelastic scattering with backscattering monochromatization. *J. Synchrotron Radiat.* **2019**, *26*, 1592–1599.

(41) Vuković, M.; Branković, Z.; Poleti, D.; Rečnik, A.; Branković, G. Novel simple mfethods for the synthesis of single-phase valentinite Sb_2O_3. *J. Sol-Gel Sci. Technol.* **2014**, *72*, 527–533.

(42) Sobalvarro, E. M. Structural studies of pyrochlore and scheelite semiconductors for solar fuel production. M.Sc. thesis, Stony Brook University, 2016.

(43) Hermann, R. In *Mossbauer Spectroscopy, in Handbook of Solid State Chemistry, Vol. 3*; Dronskowski, R., Kikkawa, S., Stein, A., Eds.; Wiley, Chapter 13, pp 443–484.

(44) Blöchl, P. E. Projector augmented-wave method. *Phys. Rev. B* **1994**, *50*, 17953–17979.

(45) Kresse, G.; Hafner, J. *Ab initio* molecular dynamics for liquid metals. *Phys. Rev. B* **1993**, *47*, 558–561.

(46) Kresse, G.; Furthmüller, J. Efficient iterative schemes for *ab initio* total-energy calculations using a plane-wave basis set. *Phys. Rev. B* **1996**, *54*, 11169–11186.

(47) Kresse, G.; Joubert, D. From ultrasoft pseudopotentials to the projector augmented-wave method. *Phys. Rev. B* **1999**, *59*, 1758–1775.

(48) Monkhorst, H. J.; Pack, J. D. Special points for Brillouin-zone integrations. *Phys. Rev. B* **1976**, *13*, 5188–5192.

(49) Grimme, S. Semiempirical GGA-type density functional constructed with a long-range dispersion correction. *J. Comput. Chem.* **2006**, *27*, 1787–99.

(50) Bučko, T.; Hafner, J.; Lebàgue, S.; Ángyán, J. G. Improved Description of the Structure of Molecular and Layered Crystals: Ab Initio DFT Calculations with van der Waals Corrections. *J. Phys. Chem. A* **2010**, *114*, 11814–11824.

(51) Björkman, T.; Gulans, A.; Krasheninnikov, A. V.; Nieminen, R. M. Are we van der Waals ready? *J. Phys. Condens. Matter* **2012**, *24*, 424218.

(52) Parlinski, K.; Li, Z. Q.; Kawazoe, Y. First-Principles Determination of the Soft Mode in Cubic ZrO_2. *Phys. Rev. Lett.* **1997**, *78*, 4063–4066.

(53) Togo, A.; Oba, F.; Tanaka, I. First-principles calculations of the ferroelastic transition between rutile-type and $CaCl_2$-type SiO_2 at high pressures. *Phys. Rev. B* **2008**, *78*, 134106.

(54) Deringer, V. L.; Stoffel, R. P.; Dronskowski, R. Vibrational and thermodynamic properties of GeSe in the quasiharmonic approximation. *Phys. Rev. B* **2014**, *89*, 094303.

(55) Eck, B. wxDragon, version 2.0.0. Aachen, 1994-2014; `http://www.ssc.rwth-aachen.de`.

(56) Lippens, P. Mössbauer isomer shifts of crystalline antimony compounds. *Solid State Commun.* **2000**, *113*, 399 – 403.

(57) Semin, G. K.; Babushkina, T. A.; Yakobson, G. G. *Primenenie yadernogo kvadrupol'nogo rezonansa v khimii (Application of Nuclear Quadrupole Resonance in Chemistry)*; Leningrad, Khimiya, 1972.

(58) Panasenko, A. E.; Zemnukhova, L. A.; Ignat'eva, L. N.; Kaidalova, T. A.; Polyakova, N. V.; Marchenko, Y. V. Phase composition of antimony(III) oxide samples of different origin. **2009**, *45*, 402–408.

(59) Long, G.; Stevens, J.; Bowen, L. 121Sb Mössbauer spectra of antimony oxides. *Inorganic and Nuclear Chemistry Letters* **1969**, *5*, 799 – 804.

(60) Stewart, D. J.; Knop, O.; Ayasse, C.; Woodhams, F. W. D. Pyrochlores. VII. The Oxides of Antimony: an X-Ray and Mössbauer Study. *Canadian Journal of Chemistry* **1972**, *50*, 690–700.

(61) Wille, H.-C.; Shvyd'ko, Y. V.; Alp, E. E.; Rüter, H. D.; Leupold, O.; Sergueev, I.; Rüffer, R.; Barla, A.; Sanchez, J. P. Nuclear resonant forward scattering of synchrotron radiation from 121 Sb at 37.13 keV. *Europhysics Letters (EPL)* **2006**, *74*, 170–176.

(62) Takeda, M.; Takahashi, M.; Ohyama, R.; Nakai, I. Antimony-121 Mössbauer spectra of antimony (III) compounds with a stereochemically active lone pair. *Hyperfine Interact.* **1986**, *28*, 741–744.

(63) Gütlich, P.; Bill, E.; Trautwein, A. *Mössbauer Spectroscopy and Transition Metal Chemistry: Fundamentals and Applications*; Springer Berlin Heidelberg, 2010.

(64) van Bürck, U.; Siddons, D. P.; Hastings, J. B.; Bergmann, U.; Hollatz, R. Nuclear forward scattering of synchrotron radiation. *Phys. Rev. B* **1992**, *46*, 6207–6211.

(65) Sturhahn, W. CONUSS and PHOENIX: Evaluation of nuclear resonant scattering data. *Hyperfine Interact.* **2000**, *125*, 149–172.

(66) Singwi, K. S.; Sjölander, A. Resonance Absorption of Nuclear Gamma Rays and the Dynamics of Atomic Motions. *Phys. Rev.* **1960**, *120*, 1093–1102.

(67) Hu, M.; Sturhahn, W.; Toellner, T.; Hession, P.; Sutter, J.; Alp, E. Data analysis for inelastic nuclear resonant absorption experiments. *Nucl. Instrum. Methods Phys. Res. A* **1999**, *428*, 551 – 555.

(68) Bahfenne, S.; Frost, R. L. A Review of the Vibrational Spectroscopic Studies of Arsenite, Antimonite, and Antimonate Minerals. *Appl. Spectrosc. Rev.* **2010**, *45*, 101–129.

(69) Kharbish, S. Raman spectra of minerals containing interconnected As(Sb)O_3 pyramids: trippkeite and schafarzikite. *J. Geosci.* **2012**, *57*, 53—62.

(70) Barucci, M.; Brofferio, C.; Giuliani, A.; Gottardi, E.; Peroni, I.; Ventura, G. Measurement of Low Temperature Specific Heat of Crystalline TeO_2 for the Optimization of Bolometric Detectors. *J. Low Temp. Phys.* **2001**, *123*, 303–314.

(71) Terashima, K.; Hashimoto, T.; Uchino, T.; Kim, S.-H.; Yoko, T. Structure and Nonlinear Optical Properties of Sb_2O_3-B_2O_3 Binary Glasses. *J. Ceram. Soc. Jpn.* **1996**, *104*, 1008–1014.

(72) Boldyreva, E.; Dera, P. *High-Pressure Crystallography: From Fundamental Phenomena to Technological Applications*; NATO Science for Peace and Security Series B: Physics and Biophysics; Springer Netherlands, 2010.

(73) Matsunaga, T.; Yamada, N.; Kojima, R.; Shamoto, S.; Sato, M.; Tanida, H.; Uruga, T.; Kohara, S.; Takata, M.; Zalden, P.; et al., Phase-Change Materials: Vibrational Softening upon Crystallization and Its Impact on Thermal Properties. *Adv. Funct. Mater.* **2011**, *21*, 2232–2239.

(74) Lee, S.; Esfarjani, K.; Luo, T.; Zhou, J.; Tian, Z.; Chen, G. Resonant bonding leads to low lattice thermal conductivity. *Nat. Commun.* **2014**, *5*.

(75) Korn, D. M.; Pine, A. S.; Dresselhaus, G.; Reed, T. B. Infrared Reflectivity of Paratellurite, TeO_2. *Phys. Rev. B* **1973**, *8*, 768–772.

(76) Wang, Z.; Kolesnikov, A. I.; Ito, K.; Podlesnyak, A.; Chen, S.-H. Pressure Effect on the Boson Peak in Deeply Cooled Confined Water: Evidence of a Liquid-Liquid Transition. *Phys. Rev. Lett.* **2015**, *115*, 235701.

(77) Cheng, Y. Q.; Daemen, L. L.; Kolesnikov, A. I.; Ramirez-Cuesta, A. J. Simulation of Inelastic Neutron Scattering Spectra Using OCLIMAX. *J. Chem. Theory Comput.* **2019**, *15*, 1974–1982.

(78) Chumakov, A. I.; Monaco, G.; Fontana, A.; Bosak, A.; Hermann, R. P.; Bessas, D.; Wehinger, B.; Crichton, W. A.; Krisch, M.; Rüffer, R.; et al., Role of Disorder in the Thermodynamics and Atomic Dynamics of Glasses. *Phys. Rev. Lett.* **2014**, *112*, 025502.

(79) Walrafen, G.; Revesz, A. *Structure and Bonding in Noncrystalline Solids*; Springer US, 2012.

(80) Stoffel, R. P.; Deringer, V. L.; Simon, R. E.; Hermann, R. P.; Dronskowski, R. A density-functional study on the electronic and vibrational properties of layered antimony telluride. *J. Phys. Condens. Matter* **2015**, *27*, 085402.

(81) Chumakov, A. I.; Rüffer, R.; Leupold, O.; Sergueev, I. Insight to Dynamics of Molecules with Nuclear Inelastic Scattering. *Struct. Chem.* **2003**, *14*, 109–119.

(82) Ogi, H.; Fukunaga, M.; Hirao, M.; Ledbetter, H. Elastic constants, internal friction, and piezoelectric coefficient of α-TeO_2. *Phys. Rev. B* **2004**, *69*, 024104.

(83) Damian, G.; Buzatu, A.; Apopei, I. A.; Szakács, I., Zsolt László v Denuț; Iepure, G.;

Bôrgâoanu, D. Valentinite and Colloform Sphalerite in Epithermal Deposits from Baia Mare Area, Eastern Carpathians. *Minerals* **2020**, *10*, 121.

(84) Rüffer, R.; Chumakov, A. Nuclear inelastic scattering. *Hyperfine Interact.* **2000**, *128*, 255–272.

(85) Cochran, W. W. *The Dynamics of Atoms in Crystals*; New York : Crane, Russak, 1973.

(86) Barron, T. H. K.; Berg, W. T.; Morrison, J. A.; Steacie, E. W. R. The thermal properties of alkali halide crystals II. Analysis of experimental results. *Proceedings of the Royal Society of London. Series A. Mathematical and Physical Sciences* **1957**, *242*, 478–492.

(87) Salter, L. The temperature variation of the scattering properties of crystals. *Advances in Physics* **1965**, *14*, 1–37.

(88) Hamzaoui, M.; Azri, S.; Soltani, M. T.; Lebullenger, R.; Poulain, M. Thermal and elastic characterization of Sb_2O_3-Na_2O-ZnO glasses. *Phys. Scr.* **2013**, *2013*, 014029.

(89) El-Mallawany, R.; Saunders, G. Elastic behaviour under pressure of the binary tellurite glasses TeO_2-$ZnCl_2$ and TeO_2-WO_3. *J. Mater. Sci. Lett.* **1987**, *6*, 443–446.

(90) Arnaboldi, C. et al. Production of high purity TeO_2 single crystals for the study of neutrinoless double beta decay. *J. Cryst. Growth* **2010**, *312*, 2999 – 3008.

(91) Coughlin, J. P. Contributions to the Data on Theoretical Metallurgy. XII. Heats and Free Energies of Inorganic Oxides. *Bureau of Mines Bull.* **1954**, *542*, 8.

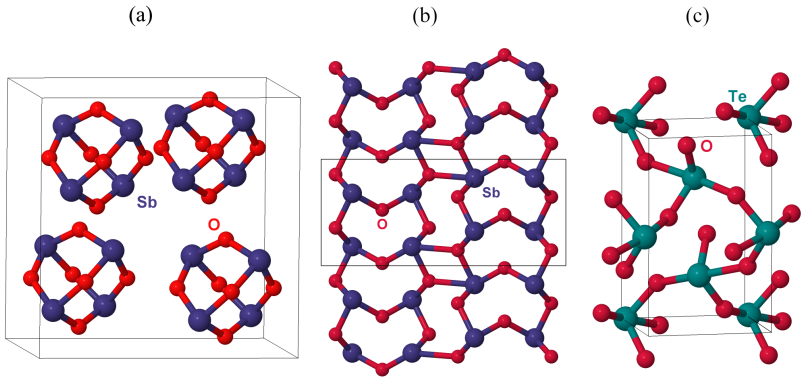

Figure 1: The crystal structure of (a) α-Sb_2O_3, (b) β-Sb_2O_3, and (c) α-TeO_2.

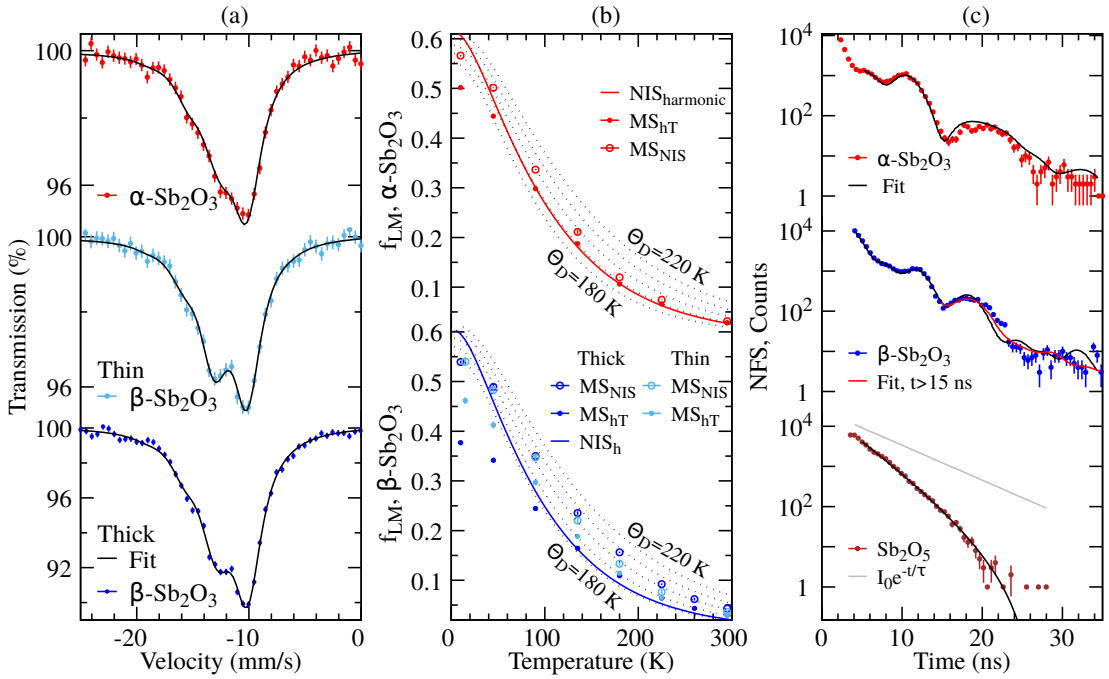

Figure 2: (a) ^{121}Sb Mössbauer absorption spectra of α- and β-Sb_2O_3 at 90 K, with comparison of a thin and thick absorber of β-Sb_2O_3. Solid lines are the corresponding fits. (b) Lamb-Mössbauer factors (f_{LM}) of α-Sb_2O_3 and β-Sb_2O_3 estimated from the relative absorption area of the Mössbauer spectra compared with the values calculated from NIS in the harmonic approximation, and with the Debye model curve between 180 and 220 K shown as reference (see text for further details). (c) NFS spectra of α-, β-Sb_2O_3 at 35 K, and Sb_2O_5 measured at 180 K. The solid black lines are the fit to the data; the red solid line in β-Sb_2O_3 shows the partial fit for $t \geq 15$ ns; the grey line indicates the exponential decay with the natural lifetime (τ =4.99 ns).

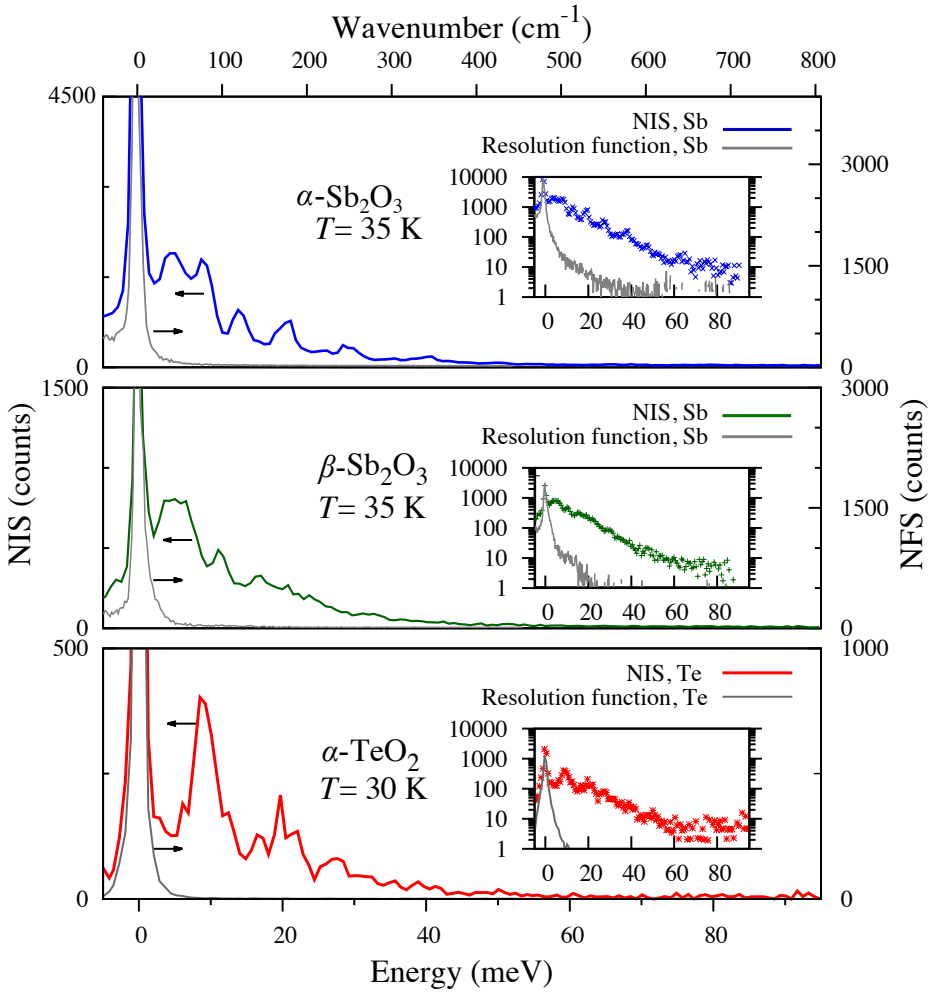

Figure 3: The element-specific ^{121}Sb and ^{125}Te NIS spectra (colored lines) and their corresponding instrumental functions (black lines) measured in (top) α-Sb_2O_3, (middle) β-Sb_2O_3, and (bottom) α-TeO_2. Insets show the same spectra in logarithmic scale. Data spread indicates error bars.

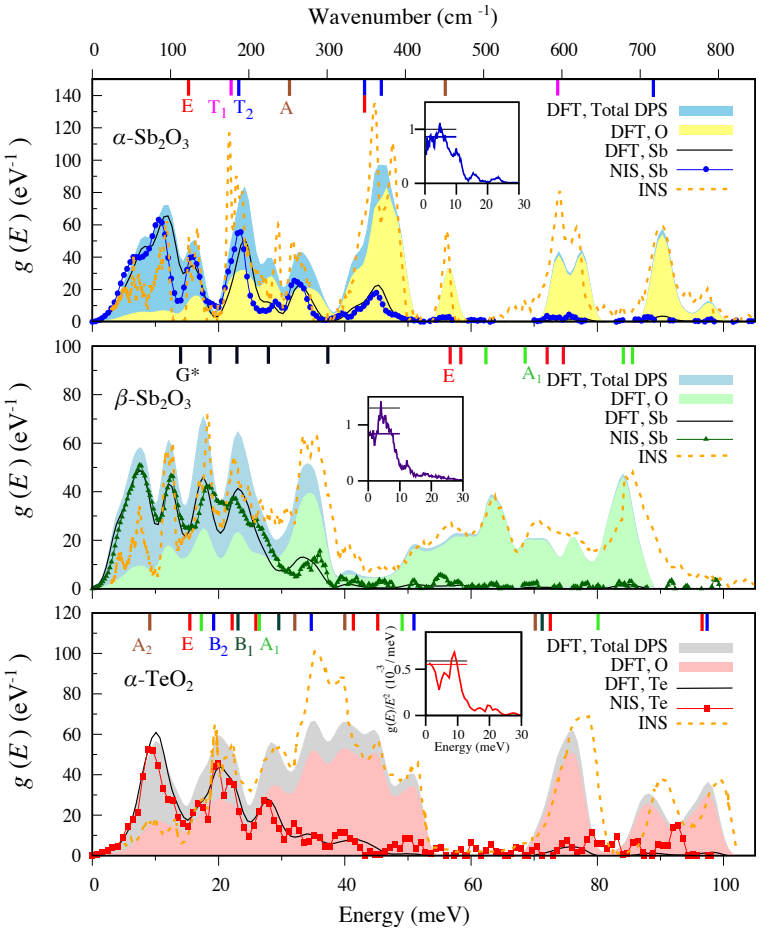

Figure 4: The experimental and calculated ^{121}Sb-DPS for (top) α-Sb_2O_3, (middle) β-Sb_2O_3, and ^{125}Te-DPS (bottom) α-TeO_2 from NIS measurements (symbols) and calculations (lines). The calculated DPS have been stretched in energy by 7% for all materials. The filled curves in all panels show the partial oxygen DPS and total DPS. The total DPS measured by inelastic neutron scattering are shown by dashed lines. The vertical colored tics represent the types of modes G* represents group modes. Each Sb and Te partial DPS spectrum is normalized to unity and the O-DPS to 1.5, 1.5, and 2 in α-Sb_2O_3, β-Sb_2O_3, and α-TeO_2, respectively. The total DPS are the sum of weighted normalized partial DPS. The INS DPS is neutron weighted and scaled for best match. The reduced DPS $g(E)/E^2$ (from the NIS result) and the low-energy fit, i.e. the estimated Debye level, are shown in the insets. The black lines are the estimated Debye levels obtained from the DFT-reduced ^{121}Sb- or ^{125}Te-DPS.).